Degradation of Commercially Available Digital Camera Images due to Variation of Rainfall Intensity in Outdoor Conditions

Akito Kanazawa[1] and Taro Uchida[2]

[1]National Institute for Land and Infrastructure Management
[2]University of Tsukuba

December 7, 2022

Abstract

Camera-based rainfall observation is a useful technology that contributes to the densification of rainfall observation networks because it can measure rainfall with high spatio-temporal resolution and low cost. To develop of practical camera-based rainfall observation technology, using the extinction coefficient as a clue, this study proposed relational Equations representing the relationship between image information, rainfall intensity, and scene depth by linking the theoretically derived rainfall intensity with a technique proposed in the computer vision field for removing static weather effects. Then, the proposed Equations were applied to outdoor images taken by commercial interval cameras at the observation site in a mountainous watershed in Japan. As a result, it was confirmed that transmission calculated from the image information decreases exponentially according to the increase in rainfall intensity and scene depth, as assumed in the proposed Equations. Therefore, the proposed Equations are generally valid even for outdoor images, and extremely important findings that will improve camera-based rainfall observation techniques were obtained. On the other hand, the calculated extinction coefficient tended to be overestimated in patches with a small scene depth, and overestimation of the extinction coefficient due to aerosol effects was also observed in the images taken during no rainfall. Although there are issues at present that need to be resolved for the technology proposed in this study, this technology has the potential to help the development of a camera-based rainfall observation technology that is accurate, robust, versatile, and accessible.

Hosted file

`essoar.10512895.1.docx` available at https://authorea.com/users/564117/articles/611100-degradation-of-commercially-available-digital-camera-images-due-to-variation-of-rainfall-intensity-in-outdoor-conditions

Akito Kanazawa[1, 2], Taro Uchida[2]

[1]National Institute for Land and Infrastructure Management, Tsukuba, Japan.

[2]Faculty of Life and Environmental Sciences, University of Tsukuba, Tsukuba, Japan.

Corresponding author: Akito Kanazawa (kanazawa.akito@gmail.com)

Key Points:

- Camera-based rainfall observation contributes to the spatio-temporal densification of rainfall observation networks.
- We proposed relational Equations representing the relationship between image information, rainfall intensity, and scene depth.
- Outdoor images obtained from field observations confirmed the validity of the proposed Equation.

Abstract

Camera-based rainfall observation is a useful technology that contributes to the densification of rainfall observation networks because it can measure rainfall with high spatio-temporal resolution and low cost. To develop of practical camera-based rainfall observation technology, using the extinction coefficient as a clue, this study proposed relational Equations representing the relationship between image information, rainfall intensity, and scene depth by linking the theoretically derived rainfall intensity with a technique proposed in the computer vision field for removing static weather effects. Then, the proposed Equations were applied to outdoor images taken by commercial interval cameras at the observation site in a mountainous watershed in Japan. As a result, it was confirmed that transmission calculated from the image information decreases exponentially according to the increase in rainfall intensity and scene depth, as assumed in the proposed Equations. Therefore, the proposed Equations are generally valid even for outdoor images, and extremely important findings that will improve camera-based rainfall observation techniques were obtained. On the other hand, the calculated extinction coefficient tended to be overestimated in patches with a small scene depth, and overestimation of the extinction coefficient due to aerosol effects was also observed in the images taken during no rainfall. Although there are issues at present that need to be resolved for the technology proposed in this study, this technology has the potential to help the development of a camera-based rainfall observation technology that is accurate, robust, versatile, and accessible.

1 Introduction

The water cycle regulates local, regional, and global climate change, and precipitation is an important component of this cycle (Eltahir & Bras, 1996). Reliable precipitation data are therefore critical for local, regional, and global water resource management and weather, climate, and hydrologic forecasting (Jiang et al., 2019; Sun et al., 2018). Rainfall is difficult to observe adequately due to large spatial and temporal variations (Kidd et al., 2016). In order to properly grasp such variations, a dense observation network is necessary on a fine temporal and spatial scale. Especially in mountainous areas where flash floods and debris flow occur, rainfall should be measured on fine spatial and temporal scales for effective early-warning against these disasters (e.g., Kidd et al., 2016). Currently, rainfall data are mainly obtained from ground observation such as rain gauge and remote sensing such as weather radar and satellites. However, rainfall data is often limited in terms of spatio-temporal resolution due to the sparseness of the ground observation networks used for both direct measurement and indirect measurement calibrations (Notarangelo et al., 2021). In addition, due mainly to the high cost of observation, a high-resolution, ground-level rainfall monitoring network has not yet been developed (Jiang et al., 2019). Therefore, innovative methods to achieve higher density in the ground-level rainfall observation network have been the focus of recent hydrological research (Tauro et al., 2018).

As an initiative to overcome the issues mentioned above, techniques have been proposed to build sensors using low-cost equipment not used for its intended use and to combine a variety of not fully utilized technologies to make opportunistic observation (Tauro et al., 2018). For these techniques, an approach has been adopted in the form of aggregating data obtained from a high-density network built using a large number of low-cost sensors that are less accurate (Notarangelo et al., 2021). While such an approach is not as accurate as conventional rain gauges in most cases, it could provide valuable additional information when combined with conventional techniques (Tauro et al., 2018). Actually, Haberlandt and Sester (2010) and Rabiei et al. (2016) reported that the idea of considering moving vehicles as rain gauges and windshield wipers as sensors to detect rainfall may enable better areal rainfall estimation than using several accurate rain gauges by making numerous observations, even if they are somewhat inaccurate. Microwave link in the cellular phone communication network, which focuses on the relationship between rain attenuation of electromagnetic signals of cellular phones transmitted from one cellular tower to another and the average rainfall along the path, have been proposed as a promising new rainfall measurement technology (Leijnse et al., 2007; Messer et al., 2006; Overeem et al., 2011; Rahimi et al., 2006; Tauro et al., 2018; Upton et al., 2005; Zinevich et al., 2009). It has been indicated that such opportunistic sensors have the potential to be utilized in geographic regions where the density of conventional rainfall measurement devices is low, namely mountainous areas and developing countries (Uijlenhoet et al., 2018). Further, since a large number of video monitoring cameras have been installed outdoors in recent years for security and safety reasons, techniques have been reported to use these cameras to estimate the environment and weather of scenes (Jacobs et al., 2009).

As techniques that use cameras to monitor surrounding conditions, techniques to grasp river levels and flow rates (Gilmore et al., 2013; Muste et al., 2008; Tauro et al., 2018), and rainfall (camera-based rain gauge) (Allamano et al. 2015; Dong et al., 2017; Jiang et al., 2019) have also been reported, and are attracting a great interest in the hydrologic field. In addition, such a camera-based technique for grasping the surrounding situation has the potential to serve as a sensor that can measure multiple types of physical quantities with a single camera, and is a very reasonable and meaningful technique for obtaining various types of information all at once. Since rainfall measurement using cameras enables the high spatio-temporal resolution and extremely low-cost measurement, it is possible to say that it has opened a novel avenue toward higher density rainfall observation (Tauro et al., 2018).

The development of camera-based rain gauges requires clarification of the effects of rainfall on images. The effects of adverse weather conditions, such as rainfall, on images have conventionally been studied mainly in the fields of computer vision and image processing (Narashimhan & Nayar, 2002). In outdoor photography systems used for monitoring, navigation, and other purposes, various algorithms such as feature detection, stereo correspondence, tracking, segmentation, and object recognition are used and these algorithms require visual clues and feature information (Garg & Nayar, 2007). Since the adverse weather conditions lead to the loss of those visual clues and feature information due to the effects of poor visibility, the objective of studies was to remove the effects of adverse weather conditions on the images and obtain clear images (Jiang et al., 2019; Tripathi & Mukhopadhyay 2014). On the other hand, in reference to such image processing techniques, studies on camera-based rain gauges quantified the degree of performance degradation due to adverse weather in outdoor photography systems as a change in weather conditions (Garg & Nayar, 2007). Such studies broadly categorize adverse weather into dynamic weather, such as rain and snow, and static weather, such as fog and haze, based on physical properties and types of visual effects (Garg & Nayar, 2007). In the case of static weather, the constituent water droplets are small, ranging from 1 to 10 m, and cannot be detected individually by a camera. The intensity produced in the pixel is therefore due to the cohesive effect of the numerous water droplets within the pixel's solid angle (Garg and Nayar, 2007). Accordingly, studies have been conducted to represent static weather and remove the effects of static weather from images by using models of atmospheric scattering such as direct attenuation and airlight (Narashimhan and Nayar, 2002, 2003). In the studies on removing static weather effects from images, methods based on priors from natural image statistics have conventionally been used (Fattal, 2008; He et al., 2011; Tan, 2008). Recently, deep machine learning-based method that extract image features from a large amount of learning data have been adopted (Qin et al., 2020; Shao et al., 2020; Zhou et al., 2021). On the other hand, in dynamic weather, water droplets are composed of particles 1,000 times larger (0.1 to 10 mm) than in static weather, and individual particles are visible to cameras. For this reason, the image processing research to remove dynamic weather effects has primarily studied techniques to extract rain by discriminating water droplets (rain streaks) from the other backgrounds, and previous studies on camera-based rain gauges are also utilizing such techniques (Bossu et al., 2011; Garg & Nayar, 2007; Luo et al., 2015).

In the previous studies, dynamic and static weather have been treated as separate themes because of the different characteristics of their effects on images. However, it has been pointed out that even in the relatively large raindrops are visible to camera, if raindrops are more than a certain distance away from the camera, individual raindrops cannot be discriminated by the camera's sensor, so rain streaks accumulate and appear as fog, i.e., the effect of static weather (Garg and Nayar, 2007; Li et al. 2018; Li et al., 2019). Therefore, in an outdoor photography system that captures images over a certain distance, the effects of static weather caused by rain as well as the effects of dynamic weather caused by rain might be considered to be expressed in the images. However, the previous studies on camera-based rain gauges have only used techniques to remove dynamic weather effects without considering static weather effects. The following issues are considered to be challenges in practical application of techniques for removing dynamic weather effects: it is effective only with stationary backgrounds in outdoor photography (Allamano et al., 2015), it requires special equipment (Dong et al., 2017), it targets only raindrops in a close range from the camera, and the fact that raindrop extraction depends on the environment surrounding the camera (Jiang et al., 2019). In other words, these techniques focusing on the effects of dynamic weather are insufficient in terms of versatility and accessibility because they require the construction of a specialized photography system for rainfall observation, and moreover, it may be difficult to obtain a variety of information other than rainfall.

Therefore, as an initial step in developing an accurate, robust, versatile, and accessible camera-based rain gauge, this study, with focus on the static weather effects of rain, analyzed the effects of rainfall intensity on the way the background is captured, i.e., the rain-induced static weather effects of images. This study proposed Equations for the relationship between image information, rainfall intensity, and the distance between the scene point and the camera (hereafter referred to as scene depth) by linking the technique of removing static weather effects reported in many computer vision studies with the theory of rainfall intensity expressed in atmospheric radiology and meteorology, using the extinction coefficient as a clue. Then, by applying the outdoor images taken by commercial interval cameras at observation sites in mountainous watersheds in Japan and rainfall observations to the proposed relational Equations, the relationship between image information, rainfall intensity, and scene depth was analyzed, and the validity of the extinction coefficient obtained from the images was verified.

This paper is structured as follows. Section 2 describes the proposed relational Equations for the relationship between image information, rainfall intensity, and scene depth. Section 3 details the outdoor observations and the processing of the captured images. Section 4 presents the results of observations, image processing, and analysis. Section 5 discusses the extinction coefficient estimated from the image information, and section 6 describes the conclusion.

2 Relational Equations for the relationship between image information, rainfall

intensity, and scene depth

2.1 Image information and extinction coefficient

Effects of static weather are mainly caused by two scattering phenomena: direct attenuation and airlight (Fattal, 2008; He et al., 2011; Narashimhan & Nayar, 2002, 2003; Tan, 2008). Light emitted from a certain background is scattered and attenuated by particles (water droplets) in the atmosphere. This phenomenon is termed as direct attenuation, which reduces the contrast of a scene (Tripathi & Mukhopadhyay, 2014). Light coming from a light source (primarily sunlight in the case of daytime outdoors) is scattered toward the camera, which results in a shift in color. This phenomenon is termed as airlight (Tripathi & Mukhopadhyay, 2014). Static weather effects can be represented as a function of the scene depth and vary spatially on a single image (He et al., 2011; Tripathi & Mukhopadhyay 2014). In the case of static weather, since the size of constituent particles (water droplets) is large compared to the wavelength of light, the "scattering coefficient", which represents the ability of a unit volume of atmosphere to scatter light in all directions, is not dependent on wavelength. For this reason, all wavelengths are equally scattered, resulting in a whitish fog (Narashimhan & Nayar, 2003). Therefore, the static weather effect that appears on the image by rainfall can be considered as a whitening of the image (increase in radiance and decrease in contrast) that depends on rainfall intensity and scene depth.

Many studies on computer vision have reported techniques for removing static weather effects from images (Fattal, 2008; He et al., 2011; Tan, 2008). In these studies, the effect of a hazy background due to fog or haze is represented by the following Image Degradation Model, using Koschmieder's model, which shows the relationship between visibility and atmospheric extinction coefficient (Fattal, 2008; Koschmieder, 1924).

$$I(x) = J(x)t(x) + A\left(1 - t(x)\right) \#(1)$$

Where, I is observed intensity, J is scene radiance, A is global atmospheric light, and t is transmission, which represents the ratio of light that reaches the camera without being scattered. x indicates the pixel position. A is independent of x and is generally constant in the single image (Tan, 2008).

In Equation (1), the right-hand side $J(x)t(x)$ is direct attenuation, A(1-$t(x)$) is airlight. Direct attenuation represents the attenuation of scene radiance by the medium in the air, while airlight represents light scattered by the myriad particles suspending in the atmosphere.

If the atmosphere is uniform, transmission t is expressed as follows.

$$t(x) = exp\left(-\beta d(x)\right) \#(2)$$

Where, d (m) is scene depth.

(m^{-1}) is called the atmospheric extinction coefficient and represents the ability of the atmosphere to dissipate light in a unit volume of atmosphere. Extinction refers to the combined effect of light scattering and absorption. In this paper, the terms extinction and scattering are used synonymously because water absorbs virtually no light in the visible light wavelength range.

Equation (2) shows that transmission attenuates exponentially according to the increase in scene depth, subject to the effect of the extinction coefficient. The principle is based on Beer-Lambert law, which means that as light passes through matter (in this case, transparent atmosphere), its intensity attenuates exponentially.

The following is a variant of Equations (1) and (2).

$$\beta = -\frac{\log_e(t(x))}{d(x)}\#(3)$$

$$\mathrm{t}(x) = \frac{A-I(x)}{A-J(x)}\#(4)$$

$$Where,\ A - J(x) \neq 0,\ and\ 0 \leq t(x) \leq 1$$

2.2 Rainfall intensity and extinction coefficient

Rainfall intensity is defined as the amount of rainfall per unit time and area (World Meteorological Organization, 2018). Therefore, rainfall intensity is expressed as follows using the particle size distribution of raindrops, raindrop volume, and falling velocity per unit volume (Uijlenhoet, 2001).

$$R = 3.6 \times 10^6 \int_0^\infty \frac{\pi D^3}{6} N(D)U(D)dD\#(5)$$

Where, R (mm h^{-1}) is rainfall intensity, D (m) is raindrop diameter, $N(D)$ (m^{-3}) is the particle size distribution of raindrops, and $U(D)$ (m s^{-1}) is the terminal falling velocity of raindrops.

Then, with the theory of atmospheric radiation, the extinction coefficient under rainfall conditions can be expressed as follows using the particle size distribution of raindrops, the surface area of raindrops projected in the optical path direction, and extinction efficiency (Grabner & Kvicera, 2011).

$$\beta = \int_0^\infty \frac{\pi D^2}{4} N(D)QdD\#(6)$$

Where, Q is called extinction efficiency and is a dimensionless parameter that expresses the ratio of the raindrop's extinction cross sectional area (a quantity that expresses the intensity of extinction of a single particle with the dimension of area) to the geometric cross sectional area of the raindrop. Under the Mie scattering theory, the extinction efficiency Q is expressed as Q=2 in terms of the relationship between raindrop size and the wavelength of visible light (Chylek, 1977; Uijlenhoet et al., 2011).

From Equations (5) and (6), both rainfall intensity and extinction coefficient can be expressed by the particle size distribution of raindrops, but analytically, rainfall intensity cannot be expressed with extinction coefficient. Then, using the relational Equations between rainfall intensity and particle size distribution (M-P distribution) presented by Marshall and Palmer (1948), the relationship between rainfall intensity and extinction coefficient is approximately linked. Using the M-P distribution, the particle size distribution of raindrops can be expressed by the following Equation.

$$N(D) = N_0 \exp(-\lambda D)\#(7)$$

$$N_0 = 8 \times 10^6\#(8)$$

$$\lambda = 4.1 \times 10^3 R^{-0.21}\#(9)$$

Where, units of N_0 and λ are m^{-4} and m^{-1}, respectively.

Substituting Equation (7) into Equation (6), we obtain:

$$\beta = \int_0^\infty \frac{\pi D^2}{4} N_0 \exp(-\lambda D) Q dD$$

$$= \tfrac{\pi N_0 Q}{4} \int_0^\infty D^2 \exp(-\lambda D) dD\#(10)$$

Here, we introduce the gamma function, which represents the generalization of the factorial.

$$\Gamma(z) = \int_0^\infty a^{z-1} \exp(-a) da = (z-1)!\#(11)$$

Applying Equation (11) to Equation (10), we obtain:

$$\beta = \frac{\pi N_0 Q}{4\lambda^3}\Gamma(3) = \frac{\pi N_0 Q}{4\lambda^3}(3-1)!$$

$$= \tfrac{\pi N_0 Q}{2\lambda^3}\#(12)$$

Substituting Equations (8) and (9) into Equation (12), extinction coefficient can be expressed as follows using rainfall intensity R.

$$\beta = \frac{8 \times 10^6 \ \mathrm{Q}}{2\left(4.1 \times 10^3 R^{-0.21}\right)^3}$$

$$= 5.80 \times 10^{-5} \ \mathrm{Q}R^{0.63} \#(13)$$

2.3 Relationship between image information, rainfall intensity, and scene depth

The extinction coefficient of the Image Degradation Model shown in Equation (3) is an extinction coefficient obtained from the image information, and if the images were taken under rainfall conditions, the coefficient will reflect rainfall intensity. On the other hand, the extinction coefficient using the rainfall intensity shown in Equation (13) is a theoretically derived value, although it is approximate, based on the atmospheric radiation theory. Therefore, by substituting Equation (13) into Equation (2), the relationship between image information, rainfall intensity, and scene depth can be obtained as follows:

$$t(x) = exp\left(-5.80 \times 10^{-5} \ \mathrm{Q}R^{0.63} d(x)\right) \#(14)$$

$$t(x) = \tfrac{A - I(x)}{A - J(x)} \#(15)$$

$$Where,\ A - J(x) \neq 0,\ and\ 0 \leq t(x) \leq 1$$

Equation (14) shows a relationship where transmission t decreases exponentially as rainfall intensity R increases and as scene depth d increases. The applicability of this relational Equation will be examined in subsequent chapters.

3 Materials and Methods

3.1 Rainfall photography and observation

We captured outdoor conditions including rainfall events and observed rainfall intensity by installing three cameras at observation sites (35° 45’ 53” N, 138° 18’ 42” E, 758 m a.s.l.) along the banks of the Omu River, which flows through Yamanashi Prefecture in central Japan. A plan view of the observation site is shown in Figure 1. Photography was taken using three commercially available interval cameras (Brinno TLC200Pro), and images of upstream, opposite bank, and downstream of the river were taken at one-minute intervals from the same point. Camera 1 took the upstream direction of the river, Camera 2 took the opposite bank direction, and Camera 3 took the downstream direction. The resolution of the image was 1280 px wide by 720 px high. The photography period was 235 days from April 19, 2021 to December 9, 2021. Images taken at night were excluded from the analysis because it was difficult to distinguish rainfall.

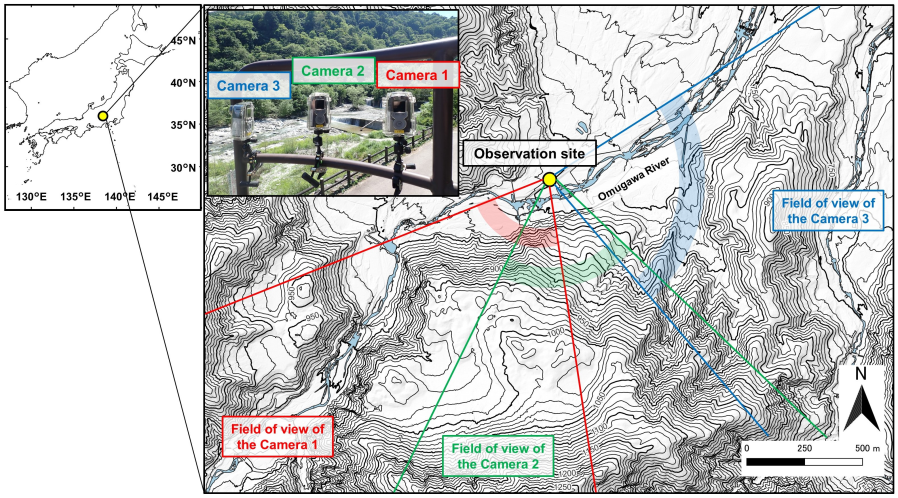

Figure 1. Observation site plan. Coastline map made with Natural Earth (2018).

One-minute rainfall intensity was also observed using a tipping bucket rain gauge (Onset RG3-M) at almost the same locations where the cameras were installed. The resolution of the tipping bucket rain gauge used was 0.2 mm. The total rainfall during the observation period was 1257 mm, and the total daytime rainfall for the analysis was 685 mm. The maximum 1-minute daytime rainfall intensity during the observation period was 0.8 mm min-1. The number of images used for the analysis by rainfall intensity is shown in Table 1.

Table 1. The number of images

Rainfall intensity	Camera 1	Camera 2	Camera 3
(mm min^{-1})			
0.0	151,823	133,970	151,771
0.2	3,141	2,908	3,141
0.4	87	75	87
0.6	21	20	21
0.8	12	12	12

3.2 Image data preprocessing and processing

For the images of landscapes taken, background objects, such as sky, vegetation, and riverbeds, and their respective scene depths are different according to the angle of view of the camera and the area of the image. Then, to analyze the influence of background objects and scene depth, patches to be analyzed were set on the image. The analysis patch was defined as the center area of 30 × 30 px in each area of the image divided into 64 areas of 8 × 8. Serial numbers were assigned to 64 patches as shown in Figure 2. The representative value of each analysis patch was the mean value of the analysis patch.

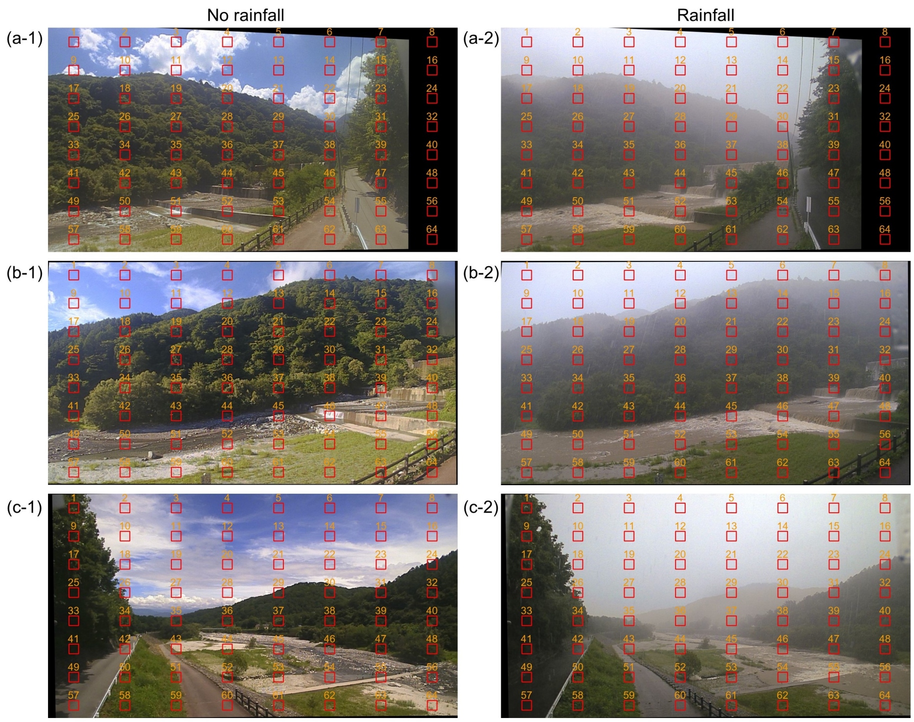

Figure 2. Analysis patches of the three cameras: (a-1), (b-1), and (c-1), respectively, show the images taken by Camera 1, Camera 2, and Camera 3 during no rainfall. Likewise, (a-2), (b-2), and (c-2) show the images taken by Camera 1, Camera 2, and Camera 3 during rainfall, respectively.

For the parameters obtained from the images to be used in Equation (15), observed intensity I was the radiance value of the image taken. Global atmospheric light A and scene radiance J were calculated from observed intensity I using the Dark Channel Prior method proposed by He et al. (2011) (hereinafter referred to as DCP). DCP is a method for recovering an image (scene radiance J) from which the effects of static weather are removed using a single hazy image (observed intensity I). The procedure for recovering scene radiance J from observed intensity I by DCP is as follows.

DCP is based on the statistical prior distribution where outdoor images without static weather effects have at least one color channel with very low intensity of some pixels in almost all non-sky patches. That is, an image that has been dilation-processed for each patch with the lowest intensity color channel values (, which is called a dark channel image) is assumed to have zero pixel values in most patches. This is expressed by the following Equation.

$$J^{\text{dark}}(x) = \min_{y\in\Omega(x)}\left(\min_{c\in\{r,\ g,\ b\}}\ \mathrm{J}^{c}(y)\right) \rightarrow 0\#(16)$$

Where, $\Omega(x)$ is a local patch centered at pixel position x, and c $\{r, g, b\}$ is the index of the color channel.

Using Equation (16), the first term on the right-hand side of Equation (17) below, which is transformed from Equation (1), can be regarded as zero.

$$\min_{y\in\Omega(x)}\left(\min_{c\in\{r,\ g,\ b\}}\frac{\mathrm{I}^c(y)}{A^c}\right)=t(x)\min_{y\in\Omega(x)}\left(\min_{c\in\{r,\ g,\ b\}}\frac{\mathrm{J}^c(y)}{A^c}\right)+1-t(x)\#(17)$$

That is, Equation (17) is transformed to the following Equation (18) when Equation (16) is applied.

$$\min_{y\in\Omega(x)}\left(\min_{c\in\{r,\ g,\ b\}}\frac{\mathrm{I}^c(y)}{A^c}\right)=1-t(x)\#(18)$$

In Equation (18), $I^c\ (y)$ is obtained from observed intensity I, so transmission t can be obtained by setting global atmospheric light A separately.

Scene radiance J can be recovered by substituting the calculated transmission t, the observed intensity I, and the global atmospheric light A, which is set separately, into Equation (1). He et al. (2011) selected pixels with the top 0.1 percent intensity in the dark channel image and set the pixel with the highest intensity of observed intensity I among these pixels as global atmospheric light A. In this study, A was calculated from observed intensity I using the same method, and scene radiance J was calculated by calculating transmission t using Equation (18). This study has adopted a method using DCP since DCP is not a machine learning-like method that requires a large amount of prior learning but is a method that can simply estimate global atmospheric light A and scene radiance J from a single image with relatively little calculation amount. In addition, since the angle of view may change even with the same camera in long-term photography, image registration was performed so that the angle of view was the same throughout the entire term. Image registration was performed by combining feature detection using the Accelerated-KAZE (Alcantarilla et al., 2013) algorithm and image warping by homography.

Scene depth d was calculated as the oblique distance from the camera to the intersection of (i) the light path in the camera's line-of-sight direction obtained from the camera's latitude, longitude, height above sea level, azimuth angle, and elevation angle information and (ii) the background 5-m digital elevation models created from the aerial laser survey data (Geospatial Information Authority of Japan, 2018). The scene depth of each analysis patch was defined as the scene depth at the center position of each patch.

The values of parameters A, J, I, and d calculated for each image were applied to the proposed relational Equations (Equations (14) and (15)) to analyze the relationship between transmission t, rainfall intensity R, and scene depth d in each analysis patch. The image processing was performed using OpenCV4.0.1, an open source library in the Python 3.8.12 programming language.

4 Results

4.1 Distribution of observed intensity I, scene radiance J, global atmospheric light A, and transmission t

Figures 3, 4, and 6 show the distribution of observed intensity I, scene radiance J, and transmission t for each rainfall intensity in each patch, respectively. Patches with a sky background were excluded from the analysis because the scene depth could not be calculated. Patches such as the rightmost patch of Camera 1, where the appropriate scene depth could not be obtained due to the image registration process, were also excluded from the analysis. Those patches not included in the analysis are indicated as $d =$ n. d. without plotting. Global atmospheric light A is set to one value per image, so values for each patch are not shown (Figure 5). Further, Table 2 shows the slope of regression line by single regression analysis in the relationship between the mean values of observed intensity I, scene radiance J, and transmission t shown for each rainfall intensity and rainfall intensity in Figures 3, 4, and 6. Although an exponential relationship between observed intensity I, scene radiance J, transmission t, and rainfall intensity is expected as shown in Equations (14) and (15), a simple regression analysis was conducted here to determine a simple trend.

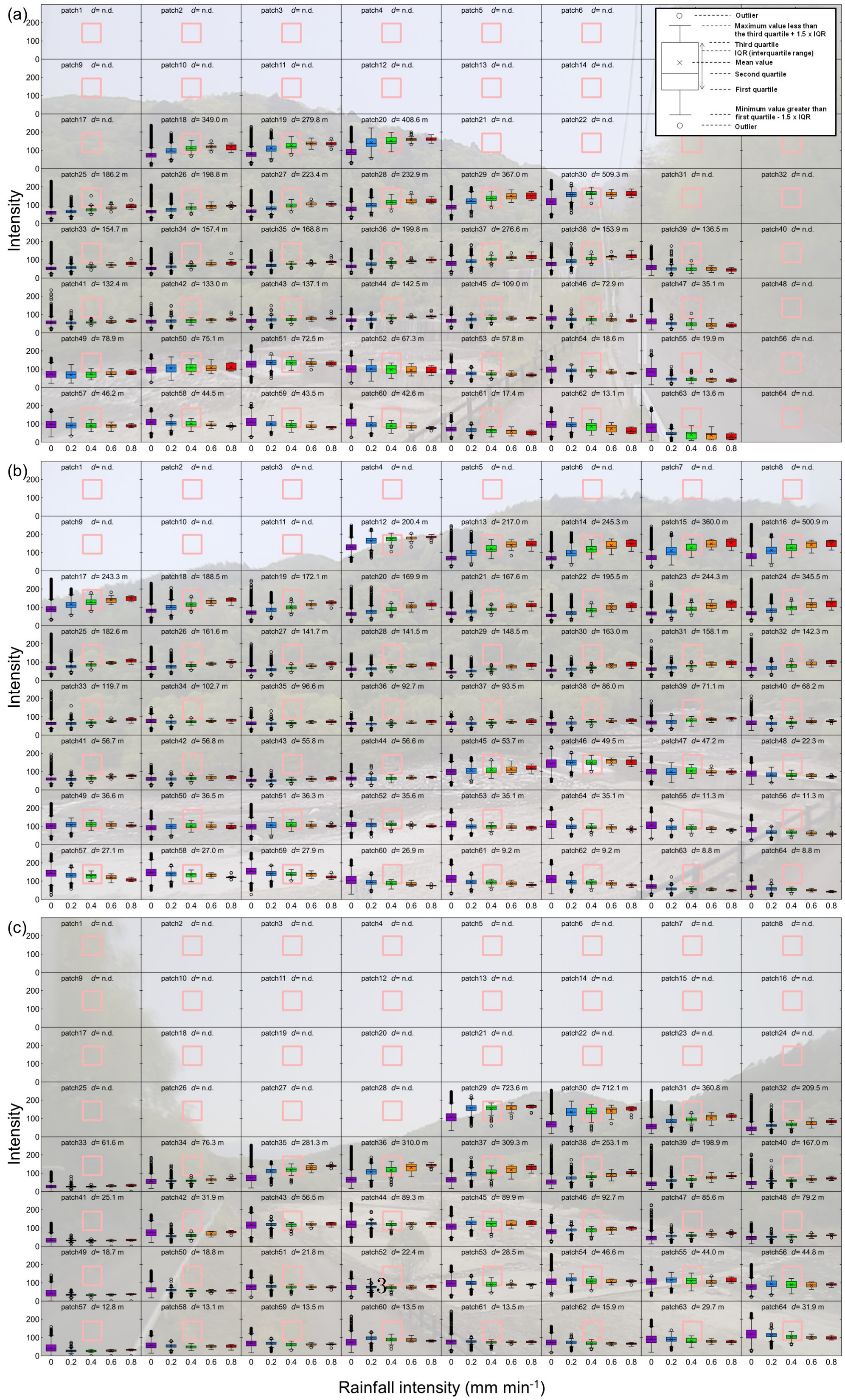

Figure 3. Distribution of observed intensity I by rainfall intensity. Each patch is marked with a patch number and scene depth: (a) Camera 1, (b) Camera 2, (c) Camera 3.

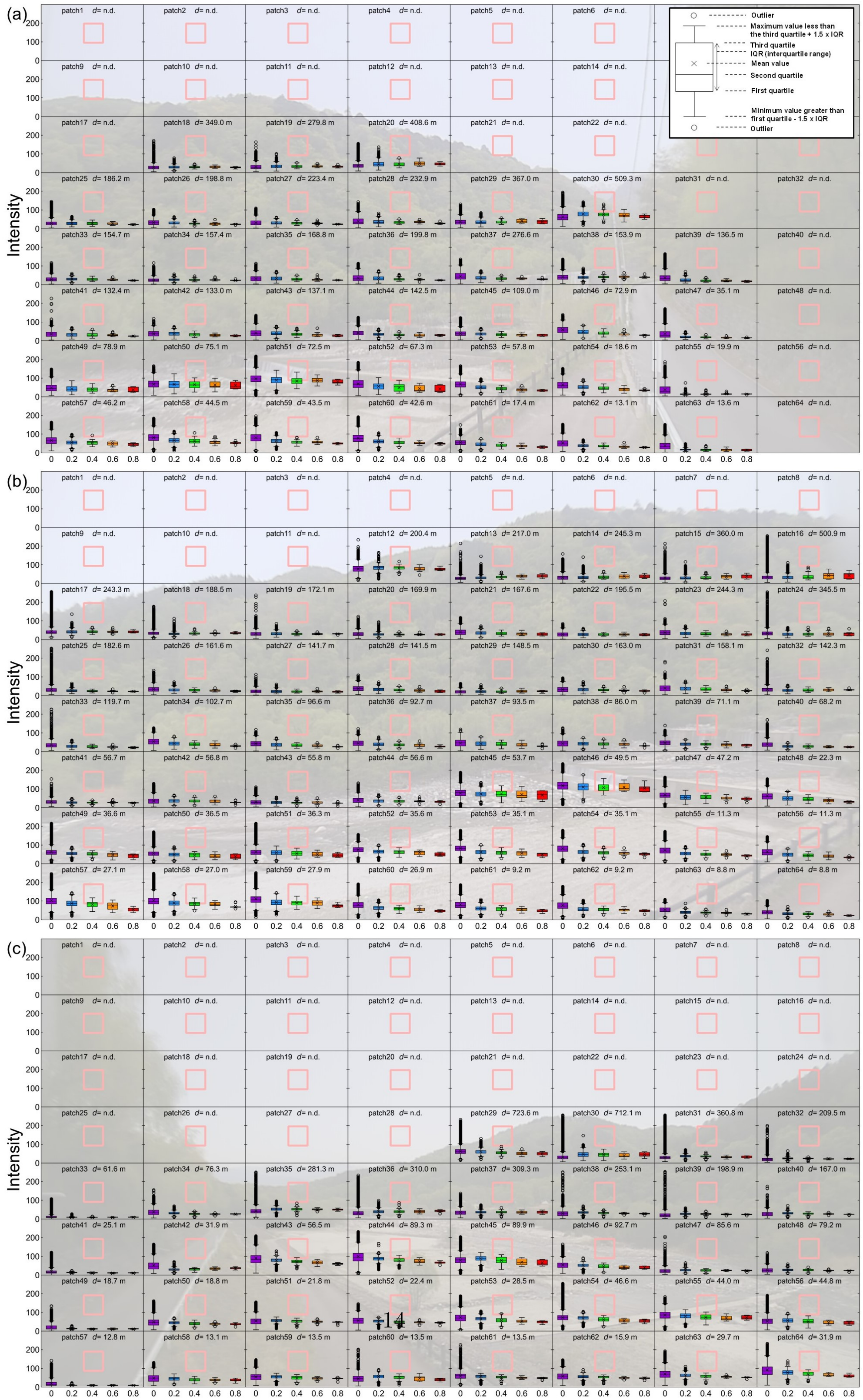

Figure 4. Distribution of scene radiance J by rainfall intensity. Each patch is marked with a patch number and scene depth: (a) Camera 1, (b) Camera 2, (c) Camera 3.

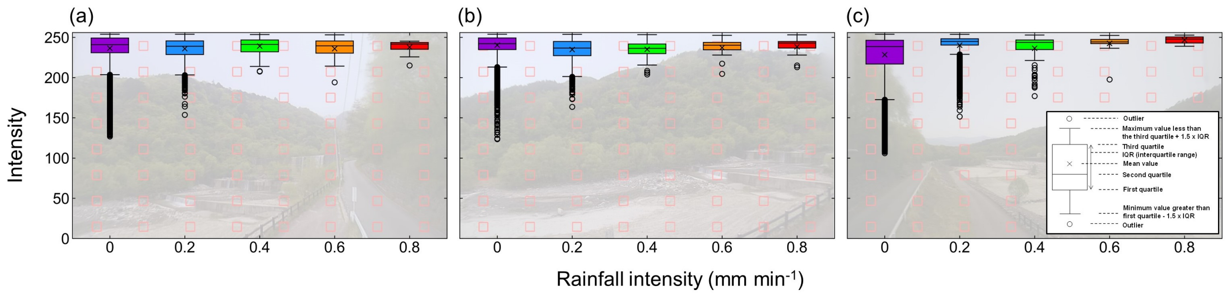

Figure 5. Distribution of global atmospheric light A by rainfall intensity: (a) Camera 1, (b) Camera 2, (c) Camera 3.

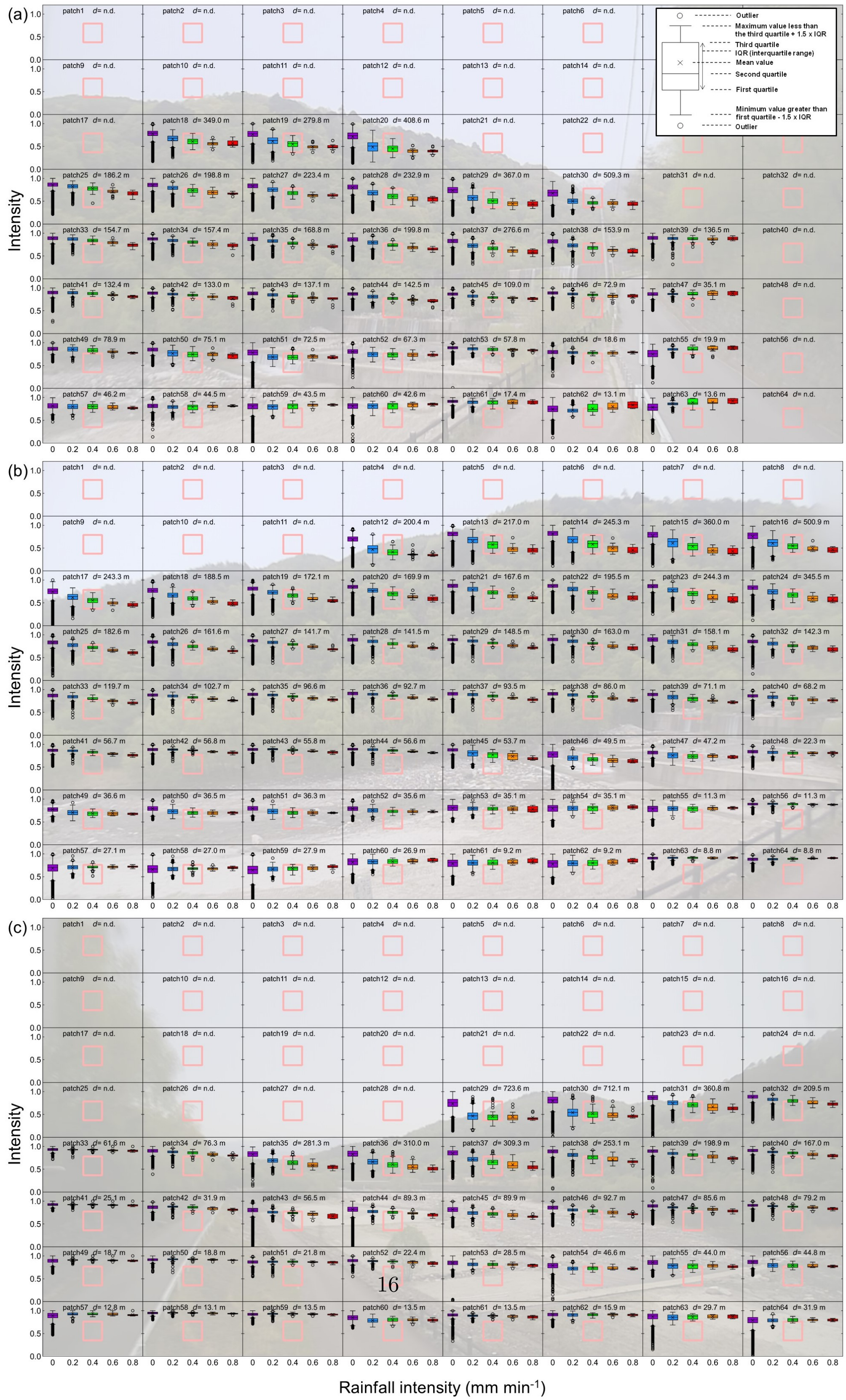

Figure 6. Distribution of transmission t by rainfall intensity. Each patch is marked with a patch number and scene depth: (a) Camera 1, (b) Camera 2, (c) Camera 3.

The value and distribution range of observed intensity I vary for each analysis patch with different background conditions (background objects and scene depth), and that the trend of changes in the value and distribution range of observed intensity I according to changes in rainfall intensity, and the slope of the regression line also vary (Figure 3 and Table 2). It was found that there exist some patches where the mean value of observed intensity I gradually increases as rainfall intensity increases in all cameras, such as patch 20 (row number 3, column number 4) in Camera 1, patch 13 (row number 2, column number 5) in Camera 2, and patch 36 (row number 5, column number 4) in Camera 3. The patch where the mean value of observed intensity I tends to increase as rainfall intensity increases is the patch where the slope is positive in Table 2, and the larger the absolute value, the more sensitive response to rainfall intensity is seen. These patches indicate that the whiteness of image increases as rainfall intensity increases on the whole.

Next, as compared to observed intensity I, the effect of rainfall intensity on scene radiance J is limited and varies little in any of the cameras (Figure 4 and Table 2).

Moreover, the intensity of global atmospheric light A is generally above 200 in all cameras, and that the effect of rainfall intensity is limited, with little variation (Figure 5).

Finally, the value and distribution range of transmission t vary according to each analysis patch with different background conditions, and that the trend of changes in the value and distribution range of transmission t according to changes in rainfall intensity and the slope of the regression line, also vary (Figure 6 and Table 2). There exist some patches where the mean value of transmission t gradually decreases as rainfall intensity increases in all cameras, such as patch 20 (row number 3, column number 4) in Camera 1, patch 14 (row number 2, column number 6) in Camera 2, and patch 36 (row number 5, column number 4) in Camera 3. The patch where the mean value of transmission t tends to decrease as rainfall intensity increases is the patch where the slope is negative in Table 2, and the larger the absolute value, the more sensitive response to rainfall intensity is seen. In other words, it can be said to quantitatively indicate that in such patches, the background is gradually becoming hazy and less visible as rainfall intensity increases.

4.2 Relationship between transmission t, rainfall intensity R, and scene depth d

Figure 7 shows the relationship between transmission t calculated by Equation (15), rainfall intensity R, and scene depth d for each patch. In all cameras, if rainfall intensity is constant, transmission t gradually decreases as scene depth increases. Similarly, if scene depth is constant, transmission will gradually decrease as rainfall intensity increases. These data clearly show that transmission t decreases exponentially according to the increase in rainfall intensity R and scene depth d, as shown in Equation (14), indicating that the proposed relationship (Equations (14) and (15)) are applicable to images taken outdoors in practice. Further, in the Figure of rainfall in each camera (rainfall intensity R is 0.2 to 0.8 mm min^{-1}), the plots generally were ranged between the theoretical lines of $Q = 0.5$ to 2.0, but in patches where scene depth d was less than approx. 100 m, the plots were often ranged below the line of $Q = 2.0$. In the patches ranged below the $Q = 2.0$ line, the ratio of scene radiance J to global atmospheric light A tends to be higher. In addition, theoretically, if there is no rainfall ($R = 0.0$ mm min^{-1}), transmission t should always be 1.0 without decreasing, but even in the case of no rainfall, transmission t tends to decrease according to distance.

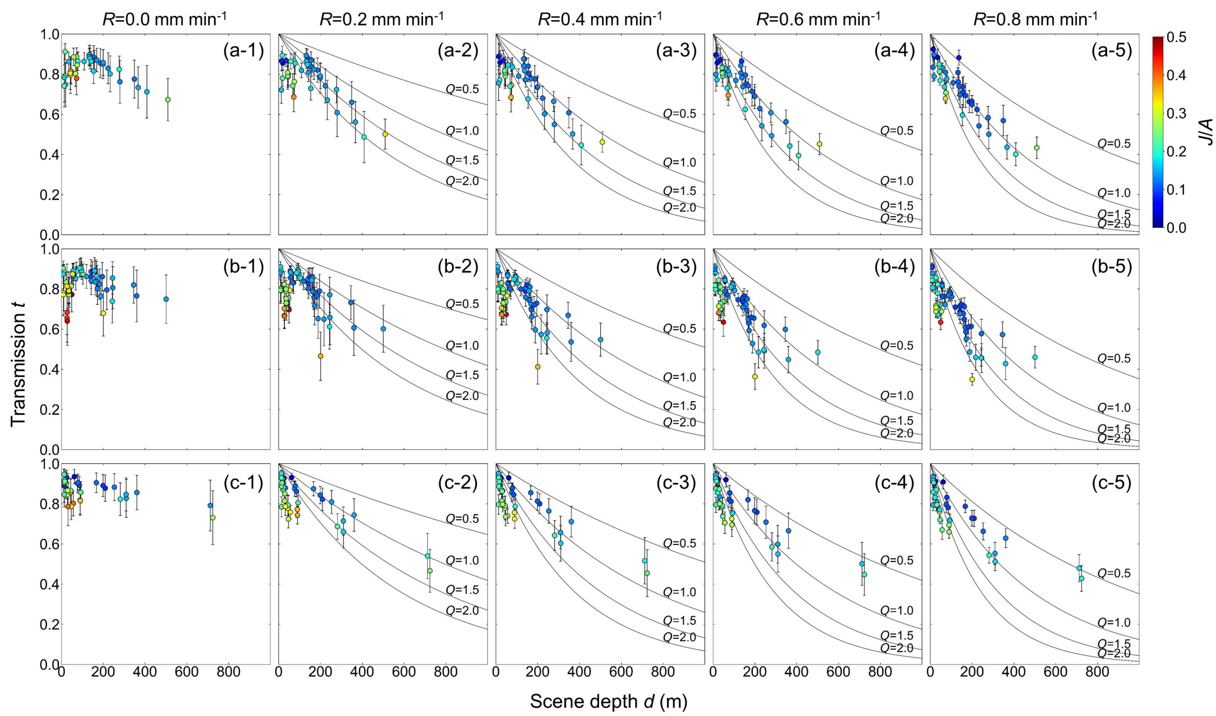

Figure 7. Relationship between transmission t and scene depth d: (a-1)–(a-5), respectively, show the results of Camera 1 by rainfall intensity ((a-1) R=0.0 mm min^{-1}, (a-2) R=0.2 mm min^{-1}, (a-3) R=0.4 mm min^{-1}, (a-4) R=0.6 mm min^{-1}, and (a-5) R=0.8 mm min^{-1}). Likewise, (b-1)–(b-5) show the results of Camera 2 by rainfall intensity, and (c-1)–(c-5) show the results of Camera 3 by rainfall intensity, respectively. The plots show the mean value of all image data in each patch, and the error bars show the standard deviation. The theoretical relationship between transmission t and scene depth d is shown as a curve when extinction efficiency Q is given in Equation (14) for four patterns: 0.5, 1.0, 1.5, and 2.0 for each rainfall intensity. The theoretical transmission t is not shown because the transmission t is always 1 when R=0.0 mm min^{-1}. Each plot is shown in a different color depending on the ratio of scene radiance J to global atmospheric light A.

5 Discussion

5.1 Factors of the value of transmission t and the variation of transmission t according to rainfall intensity

As shown in Equation (4), transmission t is determined by the relationship between observed intensity I, scene radiance J, and global atmospheric light A, but as shown in Figures 3, 4, 5, and 6, the values and trend of variation for observed intensity I, scene radiance J, global atmospheric light A, and transmission t vary according to rainfall intensity. Then, it was verified which of the factors (observed intensity I, scene radiance J, or global atmospheric light A) strongly affected the value of transmission t and the variation of transmission t according to rainfall intensity.

Figure 8 shows the relationship between (i) the mean value of observed intensity I, scene radiance J, and global atmospheric light A according to rainfall intensity in each patch for the three cameras shown in Figures 3, 4, and 5, and (ii) the mean value of transmission t shown in Figure 6. Table 3 shows the slope of the regression line and the value of the coefficient of determination R^2 obtained by simple regression analysis. Figure 8 and Table 3 clearly show a negative correlation between observed intensity I and transmission t, where transmission t decreases as observed intensity I increases in all the three cameras. In the results of the single regression analysis, the coefficient of determination was 0.47 to 0.69 in the case of no rainfall and 0.74 to 0.90 in the case of rainfall, which indicates a strong negative correlation. That is, the value of transmission t has a strong relationship with the value of observed intensity I. In addition, the absolute value of the slope of the regression line gradually increases as rainfall intensity increases, so that as rainfall intensity becomes greater, the value of transmission t tends to respond to the value of observed intensity I more sensitively and vary greater. Further, in each patch, especially in the plots where transmission t is at low values, observed intensity I increases and transmission t decreases as rainfall intensity increases. From this, it can be said that in patches where the range of variation of transmission t is large, as rainfall intensity increases, observed intensity I tends to increase, i.e., the apparent whiteness of the image increases, and transmission t tends to decrease.

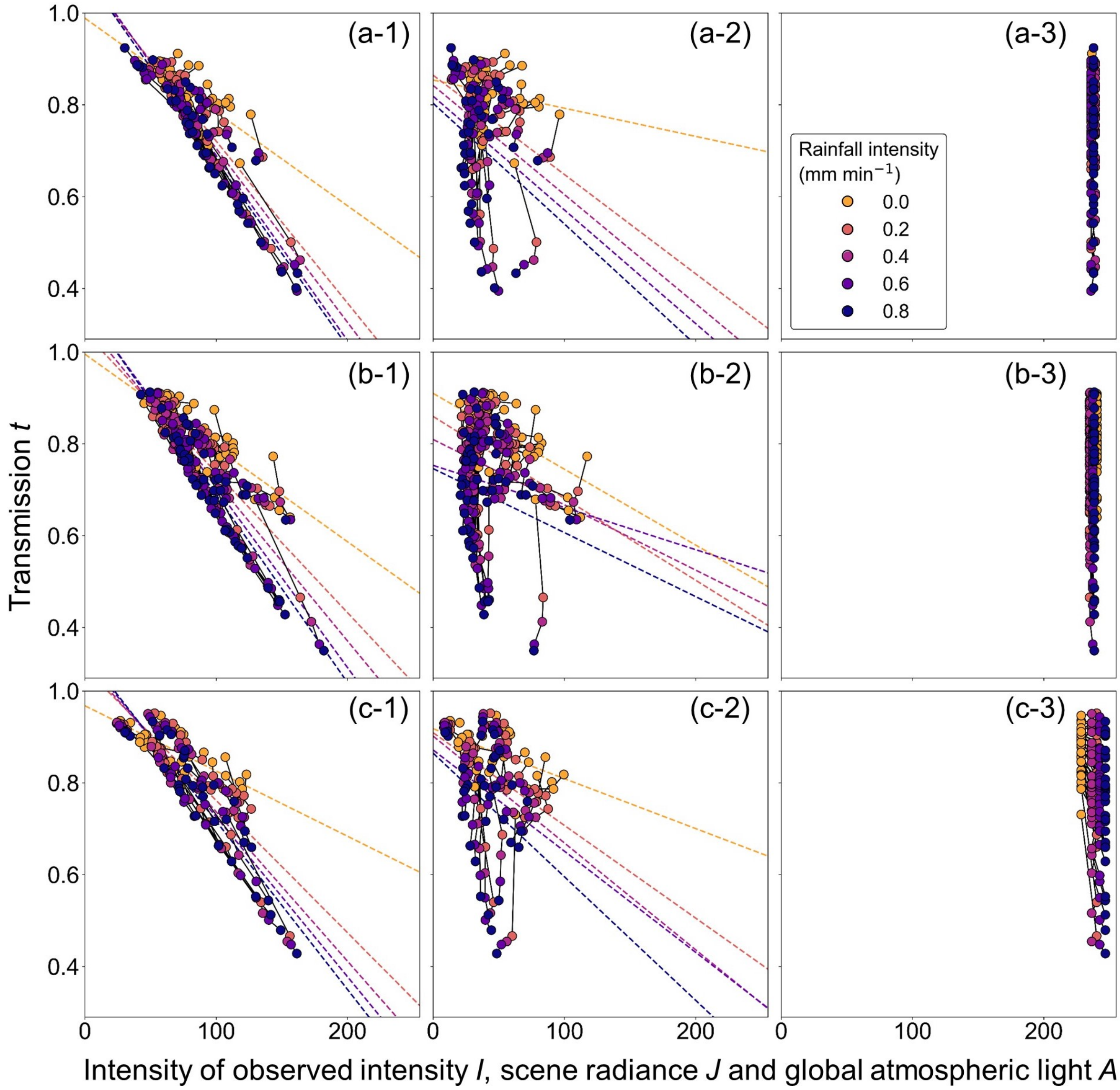

Figure 8. Relationship between observed intensity *I*, scene radiance *J*, global atmospheric light *A* and transmission *t* by analysis patch and rainfall intensity: (a-1)–(a-3), respectively, show the relationship between observed intensity *I*, scene radiance *J*, global atmospheric light *A* and transmission *t* in Camera 1. Likewise, (b-1)–(b-3) show the relationship in Camera 2, and (c-1)–(c-3) show the relationship in Camera 3, respectively. The plots by rainfall intensity for each patch were connected by straight lines to show the transition associated with changes in rainfall intensity in one patch. Global atmospheric light *A* is set to one value per image, so the values are all the same in each patch. In the Figures of observed intensity *I* and scene radiance *J*, the regression lines from the single regression analysis by rainfall intensity are shown as dotted lines that match the colors of the scatter diagram.

Next, in the relationship between scene radiance J and transmission t, the slope of the regression line was negative in all the three cameras, but the coefficient of determination was 0.04 to 0.36 in the case of no rainfall and 0.02 to 0.16 in the case of rainfall, which indicates a generally weak negative correlation or almost no correlation. In each patch, changes in scene radiance J and transmission t according to changes in rainfall intensity were also not clear. In the patch where scene radiance J is relatively high when rainfall intensity is 0.0 mm min^{-1}, scene radiance J tends to decrease as rainfall intensity increases. However, since it is not clearly linked to changes in transmission t, it can be said that the effect of changes in scene radiance J associated with changes in rainfall intensity on transmission t is limited.

Then, in the relationship between global atmospheric light A and transmission t, the relationship with transmission t and transition according to changes in rainfall intensity were not clearly found because global atmospheric light A was almost constant at 200 or more in all the three cameras.

These results suggest that the value of transmission t and the variation of transmission t according to the increase in rainfall intensity are strongly influenced mainly by the value of observed intensity I.

5.2 Validity of the extinction coefficient determined from the image

5.2.1 Values and trends of the extinction coefficient determined from the image

In this study, as shown in section 2, we linked the extinction coefficient obtained from image information with rainfall extinction coefficient approximately obtained from the atmospheric radiation theory. Since there are few examples of rainfall extinction coefficient values obtained from images in the past, the validity of the values is verified below.

Figure 9 shows the relationship between the value of extinction coefficient calculated from the image and scene depth d for each rainfall intensity. The extinction coefficient obtained from the image were calculated by Equation (3) after determining transmission t from observed intensity I, global atmospheric light A, and scene radiance J of the image, as shown in Equation (4). The Figures for each camera in the case of rainfall (rainfall intensity R is 0.2, 0.4, 0.6, 0.8 mm min^{-1}) show the cases with the extinction efficiency Q of 0.5, 1.0, 1.5, and 2.0 and the values of extinction coefficient given in the previous study to be discussed in section 5.2.2. In all the three cameras, the value of extinction coefficient in the case of no rainfall (rainfall intensity R is 0.0 mm min^{-1}) is the order of 10^{-4} to 10^{-2}, while the value of extinction coefficient in the case of rainfall is the order of 10^{-3} to 10^{-2}. In addition, in all rainfall intensities, a trend is seen that extinction coefficient decreases as scene depth increased in patchs where scene depth d is less than approx. 100 m, while it remains nearly constant when scene depth d is more than approx. 100 m. These values and trends of extinction coefficient will be discussed in the following sections.

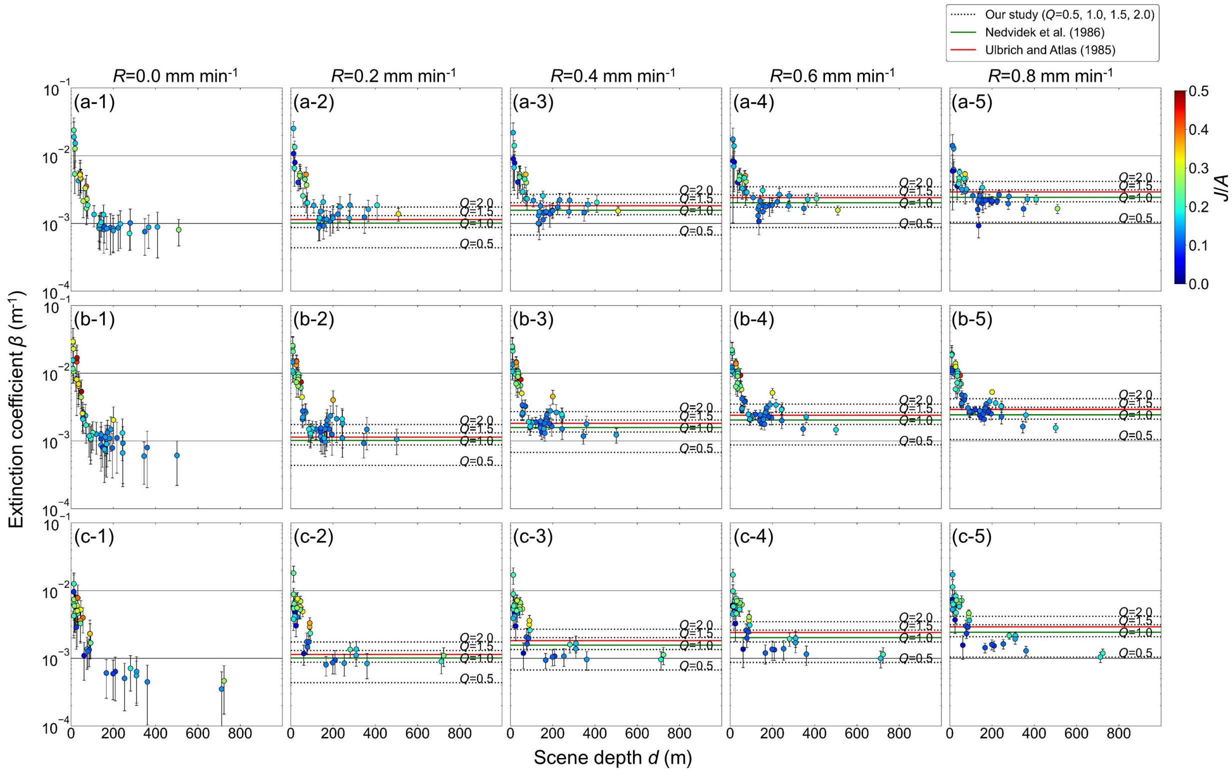

Figure 9. Relationship between extinction coefficient β and scene depth d: (a-1)–(a-5), respectively, show the results of Camera 1 by rainfall intensity ((a-1) R=0.0 mm min^{-1}, (a-2) R=0.2 mm min^{-1}, (a-3) R=0.4 mm min^{-1}, (a-4) R=0.6 mm min^{-1}, and (a-5) R=0.8 mm min^{-1}). Likewise, (b-1)–(b-5) show the results of Camera 2 by rainfall intensity, and (c-1)–(c-5) show the results of Camera 3 by rainfall intensity, respectively. The plots show the mean value of all image data in each patch, and the error bars show the standard deviation. The values of extinction coefficient β is shown as dotted lines when extinction efficiency Q is given in Equation (13) for four patterns: 0.5, 1.0, 1.5, and 2.0 for each rainfall intensity. The values of extinction coefficient β shown in previous studies is shown as green line (Nedvidek *et al.*, 1986) and red line(Ulbrich and Atlas, 1985). Each plot is shown in a different color depending on the ratio of scene radiance J to global atmospheric light A.

5.2.2 Validity of extinction coefficient in the case of rainfall determined from images

Although no research has been conducted on rainfall extinction coefficients to be obtained from images, there are many examples of obtaining extinction coefficients from the attenuation of electromagnetic waves due to rain using electromagnetic waves with wavelengths in the visible light and near-infrared regions in radar weather observation and research in the field of telecommunications(Bradley et al., 2000; Nedvidek et al., 1986; Shipley et al., 1974; Suriza et al., 2013; Ulbrich & Atlas, 1985; Zaki et al., 2019). Visible light is an electromagnetic wave with a wavelength of approx. 360 nm to 830 nm, and a camera can be regarded as a sensor that detects electromagnetic waves in that wavelength range. Uijlenhoet et al. (2011) noted that both theoretical and experimental measurements of visible light and near-infrared signal attenuation over paths ranging from a few hundred meters to several kilometers can be used to estimate the average rainfall over a path. The concept of attenuation and extinction coefficients of electromagnetic waves due to rain in such previous studies can be applicable to this study. According to the previous studies, the extinction coefficient of electromagnetic waves due to raindrops can be expressed by the following Equation (e.g., Ulbrich and Atlas, 1985).

$$\beta = \mathrm{aR}^{b}\#(19)$$

The two parameters a and b in Equation (19) represent the difference in the particle size distribution of raindrops. Applying the extinction coefficient of Equation (13) of this study to Equation (19) for the parameters a and b, we obtain $a = 5.80 \times$

10^{-5} Q, $b = 0.63$. In the previous studies, for example, Ulbrich and Atlas (1985) proposed the theoretical values $a = 2.12 \times 10^{-4}$ and $b = 0.68$ based on the results of previous experiments on rainfall intensity and optical attenuation, including the experiment of Shipley et al. 1974., and Nedvidek et al. 1986 proposed the values $a = 2.12 \times 10^{-4}$ and $b = 0.63$ based on the results of experiments using near-infrared light sources and reflectors. All the values of extinction coefficients shown in the unit of dB km^{-1} in the previous studies were converted to m^{-1}. Figure 9 shows the results of calculating the extinction coefficient using these values of a and b. The values of extinction coefficient shown in the previous studies are the order of 10^{-3}. The obtained from the images in this study in the case of rainfall is almost constant with the order of 10^{-3} in the patches where scene depth d is more than approx. 100 m, which is almost consistent with the value shown in the previous studies. Therefore, the result was that the extinction coefficient in the patches where scene depth d is more than approx. 100 m is not significantly inconsistent with the previous studies. However, in patches where scene depth d is less than approx. 100 m, the results show significant overestimation compared to the previous studies. The reasons for this overestimation are discussed in 5.2.4. As indicated in section 2, extinction efficiency Q is ideally 2 (Chylek, 1977; Uijlenhoet et al., 2011), but the values of extinction coefficient in the previous studies were ranged between 1.0 and 1.5. It has been indicated that the reason for this difference in the value of Q is that the ideal case of $Q = 2$ tends to overestimate the number of very small raindrops in the raindrop population (Bradley et al., 2000; Rogers et al., 1997).

5.2.3 Validity of extinction coefficient for in the case of no rainfall determined from images

In the case of no rainfall, as seen from Equation (13), the rain extinction coefficient approximately obtained from the atmospheric radiation theory is expected to be normally zero, and the extinction coefficient obtained from the image is also expected to be zero (synonymous with the transmission t of 1). However, as shown in the no-rainfall Figure in Figure 9 in the case of no rainfall, the extinction coefficient indicated almost the same trend in the three cameras, decreasing between the order of 10^{-2} and 10^{-3} in patches where scene depth was less than approx. 100 m, and remaining almost constant between 10^{-3} and 10^{-4} when scene depth was more than approx. 100 m. As shown in Equation (3), since extinction coefficient is a function of transmission and scene depth, the decrease in transmission t in the range where scene depth is more than approx. 100 m in the no-rainfall Figure in Figure 7 is explained by the fact that the extinction coefficient is constant in the range where scene depth is more than approx.100 m in Figure 9.

The reason why the extinction coefficient is not zero when there is no rainfall may be due to the effect of aerosols in the atmosphere. In outdoor photography, not only hydrometeors, such as rain and fog, which are the subject of this study, but also lithometeors, such as smoke and dust, degrade visibility and change the appearance of background. Therefore, even if images taken during no rainfall do not show the effects of rain, they may show the effects of hydrometeors and lithometeors that are not observed as rainfall intensity. In this paper, hydrometeors and lithometeors that are not observed as rainfall intensity are collectively referred to as aerosols.

Because of the importance of atmospheric aerosols to air pollution and the human health impacts caused by it, traffic and airport safety, and climate change, many studies have been conducted to grasp the characteristics of aerosols (Kim & Noh, 2021). Some of these studies have reported on the relationship between atmospheric aerosols and atmospheric extinction coefficients (Kim & Noh, 2021; Ozkaynak et al., 1985; Shin et al., 2022; Uchiyama et al., 2014; Uchiyama et al., 2018). Ozkaynak et al. (1985) calculated the values of extinction coefficient from the results of visibility observation in 12 airports at large cities in the U.S. and reported that they were 4.0×10^{-5} - 7.8×10^{-4}m^{-1}. Uchiyama et al. (2014) reported that the mode of extinction coefficients observed at Tsukuba, Japan, using an integrating nephelometer and one- and three-wavelength absorption spectrometers was 2.5×10^{-5} m^{-1}, and most values were not more than 2.0×10^{-4} m^{-1}. Uchiyama et al. (2018), also observed extinction coefficients in two cities, Fukuoka, Japan and Beijing, China, using an integrating nephelometer and an aethalometer, and found that the annual mean for Fukuoka was 7.46×10^{-5} m^{-1} and for Beijing, 4.12×10^{-4} m^{-1}. Further, Kim and Noh (2021) obtained the extinction coefficients of atmospheric aerosols from camera images and reported that the estimated range was 5.0×10^{-5} to 1.0×10^{-3} m^{-1} and the optimal aerosol extinction coefficient was approx. 5.0×10^{-4} m^{-1}, and Shin et al. (2022) reported that the range obtained from the camera images and visibility data was 2.0×10^{-6} to 1.1×10^{-3} m^{-1}. In reference to these reports, although there are differences in the air pollution conditions of the observation patches and the observation methods used, the value of atmospheric extinction coefficient is expected to be the order of 10^{-6} to 10^{-3} in m^{-1} unit, even if there is no rainfall, due to aerosol effects. In the results of this study, the extinction coefficient is the order of 10^{-3} to 10^{-4} in patches where scene depth is more than approx. 100 m, as shown in the no-rainfall Figure in Figure 9. This result is a slight overestimation compared to the results observed in Japan in recent years, i.e., Uchiyama et al. (2014) and Uchiyama et al. (2018), but is considered to be generally appropriate. Therefore, it would not be highly inconsistent to assume that aerosol effects are manifested in the extinction coefficient of no rainfall in patches where the scene depth is more than approx. 100 m. However, in patches where scene depth d is less than approx. 100 m, the results show significant overestimation compared to the previous studies as well as the case of rainfall.

5.2.4 Causes of overestimation of extinction coefficients obtained from images

In patches where scene depth is less than approx. 100 m, the extinction coefficients calculated from images resulted in overestimation, regardless of the presence or absence of rainfall. This implies that the static weather effect was strongly represented in the image, contrary to the fact, even though the static weather effect was actually absent or small. One possible reason for this could be the influence caused by DCP, the method used in this study to calculate extinction coefficients. DCP assumes that dark channel images of the outdoor images without static weather effects will have zero pixel values in most patches, and that transmission will decrease according to increase in scene depth and static weather effects (rainfall intensity in this study) (He et al., 2011). In other words, it is assumed that the increase in scene depth and static weather effects will make the image whiter. Therefore, it has been pointed out that there are many actual outdoor images that violate the assumption, and it is often difficult to estimate the appropriate transmission t, although DCP can properly determine transmission t if the background of the image meets the assumption (Qin et al., 2020; Qu et al., 2019; Ren et al., 2018; Wu et al., 2020). It has been reported that DCP often fails because it violates the assumed prior distribution, especially in backgrounds with white objects that are essentially similar to the color of global atmospheric light (Qin et al., 2020; Ren et al., 2018; Yang and Sun 2018).

In Figure 7 and Figure 9, the closer the ratio of scene radiance J to global atmospheric light A is to 1, the more the background has a color that is essentially similar to the color of global atmospheric light, and the more difficult it is to estimate transmission t by DCP. From Figures 7 and 9, it can be seen that in all the cameras and all rainfall intensity Figures, the values of the ratio of scene radiance J to global atmospheric light A in the patches within approx. 100m of scene depth are larger than in the patches above approx. 100m of scene depth. Therefore, many patches within approx. 100 m of scene depth were likely to violate the assumption of the expected prior distribution, which suggests that it was an inconvenient patch for the estimation of transmission. This indicates that the cause of the overestimation of the value of extinction coefficient in these patches was due to the misidentification of the white-colored background as a static weather effect, which tends to violate the DCP's assumption of prior distribution.

It has been pointed out that the ambiguity between image color and scene depth is often a problem with image fog removal techniques such as the one referenced in this study (Meng et al., 2013). In other words, the inability to determine whether the whiteness of image is due to the color of the background object itself or to the increase in scene depth is an issue for the techniques to remove static weather effects. Therefore, it is important to consider in advance the reason for the whiteness of image, even with the method proposed in this study. Since there are a number of techniques that have been proposed to express Equation (1) from images (e.g., Fattal, 2008; Tan, 2008) in addition to the method using DCP, it is a future issue to study which method can be used to obtain appropriate extinction coefficients and transmission.

In Figures 7 and 9, some plots overestimate extinction coefficients even if the value of the ratio of scene radiance J to global atmospheric light A is not necessarily larger, especially in the Figures with higher rainfall intensity. Therefore, it can be inferred that the cause of the overestimation of extinction coefficients is not only due to the effect caused by DCP. At present, other causes have not yet been identified, and the issue in the future is to determine these causes.

6 Conclusions

Using the extinction coefficient as a clue, this study proposed relational Equations representing the relationship between image information, rainfall intensity, and scene depth by linking the theoretically derived rainfall intensity with a technique proposed in the computer vision field for removing static weather effects. Then, the proposed relational Equations were applied to outdoor images taken by commercial interval cameras at observation sites in a mountainous watershed in Japan. As the result, the following findings were obtained.

(1) In the images taken outdoors, generally as shown in the proposed relational Equations, transmission t decreased exponentially according to the increase in rainfall intensity R and scene depth d.

(2) The value of transmission t and the variation of transmission t according to the increase in rainfall intensity were considered to be strongly influenced mainly by the value of observed intensity I.

(3) The extinction coefficient obtained from images during rainfall was reasonable compared to the previous studies in the patches where scene depth d was more than approx. 100 m.

(4) Extinction coefficient calculated from the no-rainfall images may have been affected by aerosols in the patches where scene depth d was more than approx. 100 m. Therefore, extinction coefficient was not zero despite the assumption from the proposed Equations.

(5) Regardless of the presence or absence of rainfall, extinction coefficients obtained from the images were overestimated in the patches where scene depth d was less than approx. 100 m. It was suggested that one of the reasons for

this was the influence caused by the method used to calculate the extinction coefficient.

Overall, these findings suggest that the relational Equations proposed in this study for image information, rainfall intensity, and scene depth, which incorporate the effects of static weather caused by rain, are generally valid even for outdoor images. On the other hand, there are still some issues to be studied, such as finding out the details of the reasons for the overestimation of extinction coefficient, methods to eliminate the overestimation, and methods to remove the effects of aerosols. Even if the proposed relational Equations are valid from a broad perspective, its applicability to a single individual image has not been verified at present. Therefore, the applicability of the proposed relational Equations to a single individual image is an issue to be addressed in the future. Thus, there are some issues that need to be resolved in the future for the technology proposed in this study. However, this technology has the potential to greatly help the development of camera-based rain gauges that are accurate, robust, versatile, and accessible. Therefore, further study needs to be promoted in order to improve sensing technology for meteorology and hydrology, and to construct a high-density rainfall observation network that can measure rainfall with high spatio-temporal resolution and at low cost.

Acknowledgments

This work was supported by JSPS KAKENHI grant number 20H03019, Fujigawa Sabo Office, Kanto Reginal Bureau, Ministry of Land, Infrastructure, Transport and Tourism.

Data Availability Statement

The images of Camera 1 and data used for analysis in this study are available at https://doi.org/10.5281/zenodo.7163149. The images of Camera 2 and Camera 3 are available at https://doi.org/10.5281/zenodo.7166150, https://doi.org/10.5281/zenodo.7166178, respectively. The observation site plan shown in Figure 1 were provided by Fujigawa Sabo Office, Kanto Reginal Bureau, Ministry of Land, Infrastructure, Transport and Tourism. The coastline map shown in Figure 1 are available at the site of Natural Earth https://www.naturalearthdata.com/downloads/10m-physical-vectors/10m-coastline/ (Natural Earth, 2018). The 5-m digital elevation models used for calculation of scene depth in this study are available at the site of the Geospatial Information Authority of Japan https://www.gsi.go.jp/kiban/index.html (Geospatial Information Authority of Japan, 2018). Part of the software associated with this manuscript for the calculation of Dark Channel Prior method is licensed under MIT and published on GitHub https://github.com/He-Zhang/image_dehaze (Zhang, 2021).

References

Alcantarilla, P. F., Nuevo, J., & Bartoli, A. (2013). Fast explicit diffusion for accelerated features in nonlinear scale spaces. *Proceedings of 24^{th} British Machine Vision Conference (BMVC)*, Bristol, UK.

Allamano, P., Croci, A., & Laio, F. (2015). Toward the camera rain gauge. *Water Resources Research*, *51*, 1744–1757. https://doi.org/10.1002/2014WR016298

Bossu, J., Hautière, N., & Tarel, J. P. (2011). Rain or snow detection in image sequences through use of a histogram of orientation of streaks. *International Journal of Computer Vision*, *93*(3), 348–367. https://doi.org/10.1007/s11263-011-0421-7

Bradley, S. G., Stow, C. D., & Lynch-Blosse, C. A. (2000). Measurements of rainfall properties using long optical path imaging. *Journal of Atmospheric and Oceanic Technology, 17*(6), 761–772. https://doi.org/10.1175/1520-0426(2000)017<0761:MORPUL>2.0.CO;2

Chylek, P. (1977). A note on extinction and scattering efficiencies. *Journal of Applied Meteorology*, *16*, 321–322.

Dong, R., Liao, J., Li, B., Zhou, H., & Crookes, D. (2017). Measurements of rainfall rates from videos. *Proceedings of 2017 10th International Congress on Image and Signal Processing, BioMedical Engineering and Informatics (CISP-BMEI)*, Shanghai, China. https://doi.org/10.1109/CISP-BMEI.2017.8302066

Eltahir, E. A. B., & Bras, R. L. (1996). Precipitation recycling. *Reviews of Geophysics, 34*(3), 367–378. https://doi.org/10.1029/96RG01927

Fattal, R. (2008). Single image dehazing. *ACM Transactions on Graphics*, *27*(3). https://doi.org/10.1145/1360612.1360671

Garg, K., & Nayar, S. K. (2007). Vision and rain. *International Journal of Computer Vision*, *75*(1), 3–27. https://doi.org/10.1007/s11263-006-0028-6

Geospatial Information Authority of Japan. (2018). The digital elevation models. [Dataset]. Geospatial Information Authority of Japan. https://www.gsi.go.jp/kiban/index.html

Gilmore, T. E., Birgand, F., & Chapman, K. W. (2013). Source and magnitude of error in an inexpensive image-based water level measurement system. *Journal of Hydrology*, *496*, 178–186. https://doi.org/10.1016/j.jhydrol.2013.05.011

Grabner, M., & Kvicera, V. (2011). The wavelength dependent model of extinction in fog and haze for free space optical communication. *Optics Express*, *19*(4), 3379–3386. https://doi.org/10.1364/oe.19.003379

Haberlandt, U., & Sester, M. (2010). Areal rainfall estimation using moving cars as rain gauges - A modelling study. *Hydrology and Earth System Sciences*, *14*(7), 1139–1151. https://doi.org/10.5194/hess-14-1139-2010

He, K., Sun, J., & Tang, X. (2011). Single image haze removal using dark channel prior. *IEEE Transactions on Pattern Analysis and Machine Intelligence*, *33*(12), 2341–2353. https://doi.org/10.1109/TPAMI.2010.168

Jacobs, N., Burgin, W., Fridrich, N., Abrams, A., Miskell, K., Braswell, B. H., Richardson, A. D., & Pless, R. (2009). The global network of outdoor webcams: Properties and applications. *ACM International Symposium on Advances in Geographic Information Systems*, 111–120. https://doi.org/10.1145/1653771.1653789

Jiang, S., Babovic, V., Zheng, Y., & Xiong, J. (2019). Advancing opportunistic sensing in Hydrology: A novel approach to measuring rainfall with ordinary surveillance cameras. *Water Resources Research*, *55*(4), 3004–3027. https://doi.org/10.1029/2018WR024480

Kidd, C., Becker, A., Huffman, G. J., Muller, C. L., Joe, P., Skofronick-Jackson, G., & Kirschbaum, D. B. (2017). So, how much of the Earth's surface is covered by rain gauges? *Bulletin of the American Meteorological Society*, *98*(1), 69–78. https://doi.org/10.1175/BAMS-D-14-00283.1

Kim, D., & Noh, Y. (2021). An aerosol extinction coefficient retrieval method and characteristics analysis of landscape images. *Sensors*, *21*(21), 7282. https://doi.org/10.3390/s21217282

Koschmieder, H. (1924). Theorie der horizontalen sichtweite. *Beitrage zur Physik der freien Atmosphare*, *12*, 171–181.

Leijnse, H., Uijlenhoet, R., & Stricker, J. N. M. (2007). Rainfall measurement using radio links from cellular communication networks. *Water Resources Research*, *43*(3), W03201. https://doi.org/10.1029/2006WR005631

Li, R., Tan, R. T. & Cheong. L.-F. (2018). Robust optical flow in rainy scenes. *Proceedings of the European Conference on Computer Vision (ECCV)*, Munich, Germany, 288– 304.

Li, S., Araujo, I. B., Ren, W., Wang, Z., Tokuda, E. K., Hirata, Jr. R., Cesar, Jr., R., Zhang, J., Guo, X., & Cao, X. (2019). Single image deraining: A comprehensive benchmark analysis. *Proceedings of the 2019 IEEE/CVF Conference on Computer Vision and Pattern Recognition (CVPR)*, Long Beach, CA, USA, 3838–3847.

Luo, Y., Xu, Y., & Ji, H. (2015). Removing rain from a single image via discriminative sparse coding. *Proceedings of the 2015 IEEE International Conference on Computer Vision (ICCV)*, Santiago, Chile, 3397–3405. https://doi.org/10.1109/ICCV.2015.388

Marshall, J. S., & Palmer, W. M. K. (1948). The distribution of raindrops with size. *Journal of Meteorology*, *5*(4), 165–166. https://doi.org/10.1175/1520-0469(1948)005<0165:TDORWS>2.0.CO;2

Meng, G., Wang, Y., Duan, J., Xiang, S., & Pan, C. (2013). Efficient image dehazing with boundary constraint and contextual regularization. *Proceedings of the 2013 IEEE International Conference on Computer Vision (ICCV)*, Sydney, NSW, Australia, 617–624. https://doi.org/10.1109/ICCV.2013.82

Messer, H., Zinevich, A., & Alpert, P. (2006). Environmental monitoring by wireless communication networks. *Science*, *312*(5774), 713. https://doi.org/10.1126/science.1120034

Muste, M., Fujita, I., & Hauet, A. (2008). Large-scale particle image velocimetry for measurements in riverine environments. *Water Resources Research*, *46*(4), W00D19. https://doi.org/10.1029/2008WR006950

Narasimhan, S.G. & Nayar, S.K. (2002). Vision and the atmosphere. *International Journal of Computer Vision*, *48*(3), 233–254. https://doi.org/10.1023/A:1016328200723

Narasimhan, S.G. & Nayar, S.K. (2003). Contrast restoration of weather degraded images. *IEEE Transactions on Pattern Analysis and Machine Intelligence*, *25*(6). 713–724. https://doi.org/10.1109/TPAMI.2003.1201821

Natural Earth. (2018). Coastline. [Dataset]. Natural Earth. https://www.naturalearthdata.com/downloads/1
physical-vectors/10m-coastline/

Nedvidek, F., Schneider, C., Kucerovsky, Z., & Brannen, E. (1986). Near-infrared extinction in rain measured using a single detector system. *Journal of atmospheric and oceanic technology*, *3*(3), 391–399. https://doi.org/10.1175/1520-0426(1986)003<0391:NIEIRM>2.0.CO;2

Notarangelo, N. M., Hirano, K., Albano, R., & Sole, A. (2021). Transfer learning with convolutional neural networks for rainfall detection in single images. *Water*, *13*(5), 588. https://doi.org/10.3390/w13050588

Overeem, A., Leijnse, H., & Uijlenhoet, R. (2011). Measuring urban rainfall using microwave links from commercial cellular communication networks. *Water Resources Research*, *47*(12), W12505. https://doi.org/10.1029/2010WR010350

Ozkaynak, H., Schatz, A. D., Thurston, G. D., Isaacs, R. G., & Husar, R. B. (1985). Relationships between aerosol extinction coefficients derived from airport visual range observations and alternative measures of airborne particle mass. *Journal of the Air Pollution Control Association*, *35*(11), 1176–1185. https://doi.org/10.1080/00022470.1985.10466020

Qin, X., Wang, Z., Bai, Y., Xie, X., Jia, H. (2020). FFA-Net: Feature Fusion Attention Network for Single Image Dehazing. *Proceedings of the AAAI Conference on Artificial Intelligence*, *34*(7), 11908–11915. https://doi.org/10.1609/aaai.v34i07.6865

Qu, Y., Chen, Y., Huang, J., & Xie, Y. (2019). Enhanced PIX2PIX dehazing network. *Proceedings of the 2019 IEEE/CVF Conference on Computer Vision and Pattern Recognition (CVPR)*, Long Beach, CA, USA, 8152–8160. https://doi.org/10.1109/CVPR.2019.00835

Rabiei, E., Haberlandt, U., Sester, M., Fitzner, D., & Wallner, M. (2016). Areal rainfall estimation using moving cars -Computer experiments including hydrological modeling. *Hydrology and Earth System Sciences*, *20*(9), 3907–3922. https://doi.org/10.5194/hess-20-3907-2016

Rahimi, A. R., Holt, A. R., Upton, G. J. G., Krämer, S., Redder, A., & Verworn, H. R. (2006). Attenuation calibration of an X-band weather radar using a microwave link. *Journal of Atmospheric and Oceanic Technology*, *23*(3), 395–405. https://doi.org/10.1175/JTECH1855.1

Ren, D., Zuo, W., Hu, Q., Zhu, P., & Meng, D. (2019). Progressive image deraining networks: A better and simpler baseline. *Proceedings of the 2019 IEEE/CVF Conference on Computer Vision and Pattern Recognition (CVPR)*, Long Beach, CA, USA, 3932–3941. https://doi.org/10.1109/CVPR.2019.00406

Rogers, R. R., Lamoureux, M. F., Bissonnette, L. R., & Peters, R. M. (1997). Quantitative interpretation of laser ceilometer intensity profiles. *Journal of Atmospheric and Oceanic Technology*, *14*(3), 396–411. https://doi.org/10.1175/1520-0426(1997)014<0396:QIOLCI>2.0.CO;2

Shao, Y., Li, L., Ren, W., Gao, C., & Sang, N. (2020). Domain adaptation for image dehazing. *Proceedings of the 2020 IEEE/CVF Conference on Computer Vision and Pattern Recognition (CVPR)*, Seattle, WA, USA, 2805–2814. https://doi.org/10.1109/CVPR42600.2020.00288

Shin, J., Kim, D., & Noh, Y. (2022). Estimation of Aerosol Extinction Coefficient Using Camera Images and Application in Mass Extinction Efficiency Retrieval. *Remote Sensing*, *14*(5), 1224. https://doi.org/10.3390/rs14051224

Shipley, S. T., Eloranta, E. W. & Weinman, J. A. (1974), Measurement of rainfall rates by lidar, *Journal of Applied Meteorology*, *13*(7), 800–807. https://doi.org/10.1175/1520-0450(1974)013<0800:MORRBL>2.0.CO;2

Sun, Q., Miao, C., Duan, Q., Ashouri, H., Sorooshian, S., & Hsu, K. L. (2018). A Review of Global Precipitation Data Sets: Data Sources, Estimation, and Intercomparisons. *Reviews of Geophysics*, *56*(1), 79–107. https://doi.org/10.1002/2017RG000574

Suriza, A. Z., Md Rafiqul, I., Wajdi, A. K., & Naji, A. W. (2013). Proposed parameters of specific rain attenuation prediction for Free Space Optics link operating in tropical region. *Journal of Atmospheric and Solar-Terrestrial Physics*, *94*, 93–99. https://doi.org/10.1016/j.jastp.2012.11.008

Tan, R. T. (2008). Visibility in bad weather from a single image. *Proceedings of the 2008 IEEE Conference on Computer Vision and Pattern Recognition (CVPR)*, Anchorage, AK, USA. https://doi.org/10.1109/CVPR.2008.4587643

Tauro, F., Selker, J., Van De Giesen, N., Abrate, T., Uijlenhoet, R., Porfiri, M., et al. (2018). Measurements and observations in the XXI century (MOXXI): Innovation and multi-disciplinarity to sense the hydrological cycle. *Hydrological Sciences Journal*, *63*(2), 169–196. https://doi.org/10.1080/02626667.2017.1420191

Tripathi, A. K., & Mukhopadhyay, S. (2014). Efficient fog removal from video. S*ignal, Image and Video Processing*, *8*, 1431–1439. https://doi.org/10.1007/s11760-012-0377-2

Uchiyama, A., Yamazaki, A., Kudo, R., Kobayashi, E., Togawa, H., & Uesawa, D. (2014). Continuous ground-based observation of aerosol optical properties at Tsukuba, Japan: Trend and climatology. *Journal of the Meteorological Society of Japan*, *92A*, 93–108. https://doi.org/10.2151/jmsj.2014-A06

Uchiyama, A., Chen, B., Yamazaki, A., Shi, G., Kudo, R., Nishita-Hara, C., Hayashi, M., Habib, A., & Matsunaga, T. (2018). Aerosol optical characteristics in Fukuoka and Beijing measured by integrating nephelometer and aethalometer: Comparison of source and downstream regions. *Journal of the Meteorological Society of Japan*, *96*(2), 215–240. https://doi.org/10.2151/jmsj.2018-026

Uijlenhoet, R. (2001). Raindrop size distributions and radar reflectivity–rain rate relationships for radar hydrology. *Hydrology and Earth System Sciences*, *5*, 615–628. https://doi.org/10.5194/hess-5-615-2001

Uijlenhoet, R., Cohard, J. M., & Gosset, M. (2011). Path-average rainfall estimation from optical extinction measurements using a large-aperture scintillometer. *Journal of Hydrometeorology*, *12*(5), 955–972. https://doi.org/10.1175/2011JHM1350.1

Uijlenhoet, R., Overeem, A., & Leijnse, H. (2018). Opportunistic remote sensing of rainfall using microwave links from cellular communication networks. *WIREs Water*, 2018; 5:e1289. https://doi.org/10.1002/wat2.1289

Ulbrich, C. W., & Atlas, D. (1985). Extinction of visible and infrared radiation in rain: Comparison of theory and experiment, *Journal of Atmospheric and Oceanic Technology*, *2*(3), 331–339. https://doi.org/10.1175/1520-0426(1985)002<0331:EOVAIR>2.0.CO;2

Upton, G. J. G., Holt, A. R., Cummings, R. J., Rahimi, A. R., & Goddard, J. W. F. (2005). Microwave links: The future for urban rainfall measurement? *Atmospheric Research*, *77*, 300–312. https://doi.org/10.1016/j.atmosres.2004.10.009

World Meteorological Organization. (2018). *Guide to Instruments and Methods of Observation (WMO-No. 8) Volume I: Measurement of Meteorological Variables*, 214. Retrieved from https://library.wmo.int/index.php?id=12407&lvl=notice_display

Wu, H., Qu, Y., Lin, S., Zhou, J., Qiao, R., Zhang, Z., Xie, Y., & Ma, L. (2021). Contrastive Learning for Compact Single Image Dehazing, *Proceedings of the 2021 IEEE/CVF Conference on Computer Vision and Pattern Recognition (CVPR)*, Nashville, TN, USA, 10551–10560.

Yang, D., & Sun, J. (2018). Proximal dehaze-net: A prior learning-based deep network for single image dehazing. *Proceedings of the European Conference on Computer Vision (ECCV)*, Munich, Germany, 702–717.

Zaki, R. W., Fayed, H. A., El Aziz, A. A., & Aly, M. H. (2019). Outdoor visible light communication in intelligent transportation systems: Impact of snow and rain. *Applied Sciences*, *9*(24), 5453. https://doi.org/10.3390/app9245453

Zhang, H. (2021). image_dehaze. [Software]. GitHub. https://github.com/He-Zhang/image_dehaze

Zhou, C., Teng, M., Han, Y., Xu, C., & Shi, B. (2021). Learning to dehaze with polarization. *Proceedings of the 35th Conference on Neural Information Processing Systems (NeurIPS 2021).*

Zinevich, A., Messer, H., & Alpert, P. (2009). Frontal rainfall observation by a commercial microwave communication network. *Journal of Applied Meteorology and Climatology*, *48*(7), 1317–1334. https://doi.org/10.1175/2008JAMC2014.1